IVYSPRING INTERNATIONAL PUBLISHER

Theranostics

2018; 8(6): 1648-1664. doi: 10.7150/thno.23369

Research Paper

2D Superparamagnetic Tantalum Carbide Composite MXenes for Efficient Breast-Cancer Theranostics

Zhuang Liu[1], Han Lin[2,3], Menglong Zhao[4], Chen Dai[5], Shengjian Zhang[1]✉, Weijun Peng[1]✉, and Yu Chen[2]✉

1. Department of Radiology, Fudan University Shanghai Cancer Center; Department of Oncology, Shanghai Medical College, Fudan University, Shanghai, 200032, P. R. China.
2. State Key Laboratory of High Performance Ceramics and Superfine Microstructure, Shanghai Institute of Ceramics, Chinese Academy of Sciences, Shanghai, 200050, P. R. China.
3. University of Chinese Academy of Sciences, Beijing, 100049, P. R. China.
4. Department of Radiology, Zhongshan Hospital, Shanghai Medical College, Fudan University, Shanghai Institute of Medical Imaging, Shanghai, 200032, P. R. China.
5. Department of Ultrasound in Medicine, Shanghai Tenth People's Hospital, Tongji University School of Medicine, Shanghai 200072, P. R. China.

✉ Corresponding authors: zhangshengjian@yeah.net (S. Zhang); cjr.pengweijun@vip.163.com (W. Peng); chenyu@mail.sic.ac.cn (Y. Chen)

Received: 2017.10.17; Accepted: 2017.12.21; Published: 2018.02.08

Abstract

Background: The emergence of two-dimensional MXenes has spurred their versatile applications in broad fields, but the exploring of novel MXene-based family members and their potential applications in theranostic nanomedicine (concurrent diagnostic imaging and therapy) have been rarely explored. In this work, we report the construction of a novel superparamagnetic MXene-based theranostic nanoplatform for efficient breast-cancer theranostics, which was based on intriguing tantalum carbide (Ta_4C_3) MXene and its further rational surface-superparamagnetic iron-oxide functionalization (Ta_4C_3-IONP-SPs composite MXenes) for efficient breast-cancer theranostic.

Methods: The fabrication of ultrathin Ta_4C_3 nanosheets was based on an exfoliation strategy and superparamagnetic iron oxide nanoparticles were *in-situ* grown onto the surface of Ta_4C_3 MXene according to the redox reaction of MXene. Ta_4C_3-IONP MXenes were modified with soybean phospholipid (SP) to guarantee high stability in physiological conditions. The photothermal therapy, contrast-enhanced CT, T_2-weighted magnetic resonance imaging and the high biocompatibility of these composite nanosheets have also been evaluated *in vitro* at cellular level and *in vivo* on mice breast tumor allograft tumor model.

Results: The Ta component of Ta_4C_3-IONP-SPs exhibits high performance for contrast-enhanced CT imaging because of its high atomic number and high X-ray attenuation coefficient, and the integrated superparamagnetic IONPs act as excellent contrast agents for T_2-weighted magnetic resonance imaging. Especially, these Ta_4C_3-IONP-SPs composite nanosheets with high photothermal-conversion efficiency (η: 32.5%) has achieved complete tumor eradication without reoccurrence, verifying their highly efficient breast-tumor photo-ablation performance.

Conclusion: This work not only significantly broadens the biomedical applications of MXene-based nanoplatforms (Ta_4C_3 MXene) by exploring their novel family members and further functionalization strategies (magnetic functionalization in this work), but also provides a novel and efficient theranostic nanoplatform for efficient breast-cancer theranostics.

Key words: Tantalum carbide, MXene, Fe_3O_4, Multimodal imaging, Photothermal therapy, Nanomedicine

Introduction

Breast cancer, one of the most common malignant cancers of women, has high incidence and mortality [1]. Early diagnosis and treatment are of significant value to breast-cancer patients. Both X-ray computed tomography (CT) and magnetic resonance imaging (MRI) play important roles in diagnosing and evaluating breast cancer. MRI is the currently recommended modality in detecting, evaluating and

diagnosing early breast lesions due to its high sensitivity and soft-tissue contrast, while CT is regarded as one of most powerful techniques for the detection of metastases with high resolution [2, 3]. For clinical practice, the multimodal-imaging techniques can overcome the intrinsic limitations by combining the unique advantages of single modality [4]. Nanoparticles are offering exciting possibilities to integrate different contrast medias in detection of tumors and their metastases, and fulfill multimodal-imaging requirements. Especially, the development of multifunctional agents with imaging capabilities as well as intrinsic therapeutic property has been becoming highly crucial, desirable and even necessary.

Currently, two-dimensional (2D) nanomaterials have attracted great attention and become an important branch of theranostic nanomedicine due to their unique ultra-thin nanostructure and physiochemical property [5-9]. Since the discovery of graphene [10, 11], a variety of 2D nanomaterials have gained increasing research interest in cancer diagnosis and treatment [12-19]. Among them, MXene, a new emerging member of 2D nanomaterials, which represents a category of transition metal carbides and carbonitrides, has attracted significant interest of scientific community in the field of biomedicine [20-24]. MXene is typically fabricated by etching out A-layer from ternary-layered carbides of MAX phases, in which M includes an early transition metal carbide, such as Ti, Ta, Mo, Nb, V, and Zr. A stands for an A-group element and X is carbon or nitrogen [25]. The unique physiochemical property of 2D materials endows them particular applications in biomedicine, such as photothermal/photodynamic therapy [16, 18], molecular imaging [26], biosensing [27] and antibacterial activity [28]. Recently, we and other groups have discovered that the ultrathin 2D Ti_3C_2 MXene could ablate tumor tissue by means of its intrinsic high photothermal-conversion performance [29, 30]. This therapeutic modality is termed as photothermal therapy (PTT), which has been developed as an intriguing cancer-therapeutic modality to ablate tumor tissues by transferring the absorbed optical energy to thermal energy by light-absorbing photothermal agents (PTAs). Assisted with PTAs, photothermal-conversion efficacy can be substantially enhanced, which means that the heat can be only generated in the tumor sites in the presence of accumulated PTAs rather than the normal tissues, causing significantly mitigated side effects [31, 32].

Recent developments of 2D Ti_3C_2 MXene have shown their high performance in biomedicine [17, 18, 26-28, 33]. It is highly encouraging and expecting that other 2D MXene-based family members might also have the potential applications in biomedicine, even with certain novel properties, biological effects and applications that mostly-explored Ti_3C_2 MXene does not have. In addition, the functionalization of MXenes can endow them with novel physiochemical properties to meet the specific biomedical requirements and broaden the application potentials and fields, which has seldom been explored yet.

In this work, we report on a superparamagnetic tantalum carbide (Ta_4C_3)-based composite MXene for concurrent MR/CT dual-modality imaging and photothermal hyperthermia of breast cancer. 2D Ta_4C_3 MXene was chosen based on three considerations. First, Ta element intrinsically has high atomic number (Z) of 73 and high X-ray attenuation coefficient (Ta: 4.3 $cm^2\ kg^{-1}$ at 100 eV), which can act as the contrast agent for contrast-enhanced computed tomography (CT) and superior to traditional Au nanoparticles with the X-ray attenuation coefficient of 5.16 cm^2/kg at 100 eV [34-38]. Second, similar to traditional Ti_3C_2 MXene, 2D Ta_4C_3 MXene shows high photothermal-conversion capability for potential PTAs-enhanced photothermal tumor ablation. Third, the abundant surface chemistry of 2D Ta_4C_3 MXene makes the possibility for further multifunctionalization. This work has successfully *in-situ* grown superparamagnetic iron oxide nanoparticles (IONPs) onto the surface of 2D Ta_4C_3 MXene (designated as Ta_4C_3-IONP) to endow these novel MXenes with contrast-enhanced T_2-weighted MR imaging capability. The unique theranostic functionality of Ta_4C_3-IONP has been systematically evaluated at both *in vitro* intracellular level and *in vivo* breast-cancer tumor allograft on mice. Especially, the biocompatibility and biosafety of these superparamagnetic Ta_4C_3-IONP composite nanosheets have been evaluated *in vivo* for guaranteeing their further potential clinical translation.

Materials and Methods

Materials

Precursor tantalum (Ta), aluminum (Al) and graphite (C) powder were purchased from Alfa Aesar, Ward Hill, USA. Soybean phospholipid (L-α-Phosphatidylcholine from soybean, Type II-S, 14-23% choline basis, noted as SP) was purchased from Sigma-Aldrich (Shanghai). Ferrous sulfate ($FeSO_4 \cdot 7H_2O$), ammonia solution, chloroform, HF solution (40%) and ethanol were obtained from Sinopharm Chemical Reagents Co., Ltd. (Shanghai). Phosphate buffer solution (PBS) was purchased from Shanghai Double-Helix Biotech Co. Ltd. trypsin-EDTA (0.25%), fetal bovine serum (FBS), Dulbecco's Modified Eagle's Medium (DMEM,

GIBCO, Invitrogen) and penicillin streptomycin were purchased from GIBCO. Calcein-AM, propidium iodide (PI) and cell counting Kit-8 (CCK-8) were obtained from Dojindo Molecular Technologies. Other regents and solvents used as received without further purification. Deionized water was used to prepare all the solutions.

Synthesis of 2D Ta_4C_3 Nanosheets (MXenes)

Ultrathin Ta_4C_3 nanosheets were fabricated according to a liquid exfoliation method based on HF etching and subsequent probe sonication of Ta_4AlC_3 bulk. Typically, Ta_4AlC_3 ceramics bulk was mixed by Ta, Al and C powders at molar ratio of 4:1.75:3. Subsequently, the mixture was ball-milled for 10 h and pressed into cylindrical discs under pressure of 50 MPa. Then, these discs were sintered at 1500 °C under argon flowing for 2 h. Ta_4AlC_3 was etched by 40% HF solution at room temperature for 3 days to remove the Al layer, followed by centrifugation at 15000 rpm for 20 min with ethanol and deionized water for three times. Ultrathin Ta_4C_3 nanosheets were re-suspended in the oxygen-free water or organic solvent for further use.

Synthesis of Ta_4C_3-IONP composite nanosheets

The Ta_4C_3-iron oxide nanoparticles composite (Ta_4C_3-IONPs) were prepared using a facile, repeatable *in-situ* growth of superparamagnetic IONPs onto the surface of nanosheets. In brief, Ta_4C_3 (1 mmol L^{-1}, 0.1 mL), $FeSO_4 \cdot 7H_2O$ (0.5 mmol L^{-1}, 0.1 mL) and ammonia solution (1 mL) were dissolved in deionized water (10 ml). Then, the mixture solution was magnetically stirred at room temperature for 4 h. The dispersion was then centrifuged for 15 min at 20,000 rpm and washed with deionized water for three cycles.

Synthesis of Ta_4C_3-IONP-SP composite nanosheets by surface SP modification

Ta_4C_3-IONPs composite nanosheets were encapsulated with soybean phospholipid (SP) to guarantee relatively high stability in physiological environments and no significant toxicity both *in vitro* and *in vivo*. Firstly, Ta_4C_3-IONP (1 mg) was added into chloroform (20 mL) containing SP (1 mg) by stirring at room temperature for 5 min. Then, the mixture was incubated at 60 °C in a rotary evaporator for 30 min to remove organic solvent. Finally, the product was re-suspended in water or phosphate buffer saline (PBS) solution for further use.

Characterization

Transmission electron microscopy (TEM), high resolution transmission electron microscopy (HRTEM) and electron energy loss spectroscopy (EELS) were taken on a JEM-2100F electron microscope operated at an acceleration voltage of 200 kV. Scanning electron microscopy (SEM) and X-ray energy dispersive spectroscopy (EDS) was conducted on a field-emission Magellan 400 microscope (FEI Company). Fourier transform infrared (FTIR) was acquired on Nicolet iS 10 (Thermo Scientific). X-ray photoelectron spectroscopy (XPS) was performed on an ESCALAB 250Xi X-ray photoelectron spectroscopy (Thermal Scientific). Hysteresis loop test was performed on MPMS-XL apparatus (Quantum Design). UV-Vis-NIR spectra were recorded on a UV-3101PC Shimadzu spectroscope. Dynamic light scattering (DLS) measurement and zeta-potential analyses were obtained on Nano-Zetasizer (Nano ZS90). X-ray diffraction (XRD) was obtained on a Rigaku D/MAX-2200 PC XRD system. NIR laser was obtained on high power of 808 nm multimode pump laser (Shanghai Connect Fiber Optics Company). The temperature and thermal images were obtained on an infrared thermal imaging instrument (FLIR™ A325SC camera, USA). The concentrations of samples were determined by inductively coupled plasma atomic emission spectrometer (ICP-AES, Agilent Technologies, US). The confocal laser scanning microscopy (CLSM) images were recorded on FV 1000 (Olympus Company, Japan). The *in vitro* and *in vivo* MR imaging evaluations were conducted on a 3.0 T clinical MRI scanner (GE Signa 3.0 T). The *in vitro* and *in vivo* CT imaging evaluations were conducted on a 64-slice scanner (Siemens SOMATOM Sensation).

In vitro photothermal performance of Ta_4C_3-IONP-SP composite nanosheets

In vitro photothermal performance of Ta_4C_3-IONP-SP composite nanosheets with varied concentrations (water, 25, 50, 100, 200 ppm) were irradiated under the 808 nm laser with the power density of 1.5 W cm^{-2}. According to the Lambert-Beer law [16], the extinction coefficient $\alpha(\lambda)$ of Ta_4C_3-IONP composite nanosheets is obtained.

$$A(\lambda)/L=\alpha C \qquad (1)$$

A is the absorbance at a wavelength (λ), a is the mass extinction coefficient at a wavelength (λ), L is path-length (1 cm), and C is the concentration of the Ta_4C_3-IONP composite nanosheets (g L^{-1}). The extinction coefficient α is determined by plotting the slope (in L g^{-1} cm^{-1}) of each linear fit against wavelength.

According to previous report [39], the photothermal conversion efficiency (η) was calculated *via* following equation:

$$\eta = \frac{hS(T_{max}-T_{surr})-Q_S}{I(1-10^{-A})} \quad (2)$$

Where h means heat transfer coefficient. S is surface area of the cell. T_{max} represents the maximum steady-state temperature. T_{surr} means ambient temperature of surrounding. Q_S represents heat dissipated from light absorbed by the cell, which is measured to be 0.27 mW. I means laser power (500 mW), A is absorbance of Ta_4C_3-IONP composite nanosheets at the excitation wavelength of 808 nm, which is calculated to be 0.27 (Figure 4E).

Then, we define θ as the following equation:

$$\theta = \frac{T-T_{surr}}{T_{max}-T_{surr}} \quad (3)$$

Where $(T - T_{surr})$ means the temperature increased compare to the surrounding, and $(T_{max} - T_{surr})$ represents the temperature change at the maximum steady-state temperature.

$$\tau_s = -\frac{t}{ln\,\theta} \quad (4)$$

τ_s represents the sample system time constant, which can be calculated to be 230 s according to the linear curve fitting of temperature cooling time in Figure 4D.

$$hS = \frac{m_s C_s}{\tau_s} \quad (5)$$

m_s (0.3g) and C_s (4.2 J g^{-1}) represent the mass and heat capacity of solvent, respectively. Putting this value into equation (5), the final photothermal-convention efficiency (η) of Ta_4C_3-IONP composite nanosheets can be calculated to be 32.5%.

In vitro cell experiment

Murine breast cancer 4T1 cells were obtained from Shanghai Institute of Cells, Chinese Academy of Sciences and cultured in normal Dulbecco's Modified Eagle's Medium (DMEM) with 10% fetal bovine serum (FBS) and 1% penicillin/streptomycin solution at 37 °C in a humidified atmosphere of 5% CO_2 incubator.

For *in vitro* cytotoxicity evaluation, 4T1 cells were seeded into 96-well plates (Corning, USA) at a density of 5 × 10^3 cells per well for 12 h. Then cells were incubated with varied concentrations of Ta_4C_3-IONP-SP composite nanosheets (e.g. 0, 12.5, 25, 50, 100, 200 ppm) for 24 h. Then, the relative cell viabilities were determined using the standard the typical Cell Counting Kit-8 (CCK-8) assay.

For the *in vitro* photothermal cancer ablation, 4T1 cells were seeded into 96-well plates with a density of 5 × 10^3 cells per well for 12 h. After further treating with different concentrations of Ta_4C_3-IONP-SP composite nanosheets (e.g. 0, 12.5, 25, 50, 100, 200 ppm) for 4 h, the cells were washed with PBS to remove the free products. Then, the 96-well plates were irradiated under an 808 nm laser at a power density of 1.5 W cm^{-2} for almost 10 min. The standard CCK-8 test was designed to determine the cell viabilities. Significant differences against the untreated control group observed with a *95% or **99% level of confidence were determined with a t-test.

For CLSM imaging, 4T1 cells were seeded into a CLSM-specific dish with a density of 70%-90% for 12 h. Subsequently, the cells were incubation with or without Ta_4C_3-IONP-SP composite nanosheets (200 ppm) for 4 h, and washed three cycles with PBS. Then the cells were irradiated under the 808 nm laser at a power density of 1.5 W cm^{-2} for about 5 min. Finally, the cells were co-stained with Calcein-AM and propidium iodide (PI) for 15 min and then washed three times with PBS. CLSM apparatus was applied to obtain the fluorescence images of living cells and dead cells. For intracellular endocytosis evaluation, the culture medium of un-stained cells was replaced with FITC-Ta_4C_3-IONP-SPs (1 mL, 100 μg $^{-1}$), which were then co-incubated for 0, 1, 2, 4 and 6 h, respectively. DAPI dye was added into the dish to stain the cell nuclei and the cells were washed with PBS for three times after staining for 15 min before observation by CLSM.

In vivo animal experiment

Healthy Kunming mice (4 weeks, female) and BALB/c nude mice (4 weeks, female) were purchased from Shanghai SLAC Laboratory Animal Co. Ltd and were maintained in a specific pathogen-free (SPF) environment during the time of the experiments in Department of Laboratory Animal Science, Fudan University. All animal experiments were in agreement with the guidelines of the Institutional Animal Care and Use Committee (IACUC) guidelines and ensured the humane care of animals.

Kunming mice were randomly divided into four groups (n = 5), and intravenously administered with Ta_4C_3-IONP-SPs at elevated doses (5, 10, 20 mg kg^{-1}), and then mice receiving the same volume of PBS were taken as control group. During the one-month period, the body weight of mice was measured every other day and no significant behavioral changes were observed in four groups. At the 30th day post-injection, those mice were sacrificed and tissues of heart, liver, spleen, lung, and kidney were collected for hematoxylin and eosin (H&E) staining analyses to monitor the histological changes. The blood samples were collected for blood biochemistry assay.

Mice breast tumor allograft was established by subcutaneous injection 4T1 tumor cells (1 × 10^7) in PBS

(200 μL) into the right hind limb of BALB/c nude mice. When the tumor volume reached almost 50 mm^3, the mice were randomly divided into four groups (n = 5): (i) *i.v.* injected with 200 μL of PBS taken as control group, (ii) *i.v.* injected with PBS (200 μL) and irradiated by 808-laser at the power density of 1.5 W cm^{-2} for 10 min taken as laser only group, (iii) *i.v.* injected with 200 μL of Ta_4C_3-IONP-SPs (20 mg mL^{-1}) taken as Ta_4C_3-IONP-SPs only group, and (iv) *i.v.* injected with 200 μL of Ta_4C_3-IONP-SPs (20 mg mL^{-1}) and irradiated by 808-laser at the power density of 1.5 W cm^{-2} for 10 min taken as laser irradiation post-injection of Ta_4C_3-IONP-SPs group. The surface temperature and thermal images of the irradiated mice were performed by an infrared thermal imaging instrument. After different treatments, the tumor size and body weight of mice was measured every 2 days for 14 days. The tumor volume was calculated in accordance with the following formula: the volume = (tumor length) × (tumor width)^2/2. Two days after various treatments, the tumor were collected to make H&E, terminal deoxynucleotidyl transferase dUTP nick end labeling (TUNEL) and Antigen Ki-67 immunofluorescence staining according to the manufacturer's protocol.

Biodistribution of Ta_4C_3-IONP-SPs composite nanosheets in tissues of interest (heart, liver, spleen, lung and kidney) and tumor was acquired on 4T1-bearing female nude mice (n = 6). Mice were sacrificed after injection of Ta_4C_3-IONP-SPs (20 mg mL^{-1}) for 24 h. Dissected tissues and tumor were weighed and homogenized, and Ta_4C_3-IONP-SPs distribution was calculated as the percentage of injected dose per gram of tissue. In addition, the excretion assessment was conducted after the intravenous injection of Ta_4C_3-IONP-SPs into health Kunming mice.

Blood circulation of Ta_4C_3-IONP-SPs composite nanosheets *in vivo* was performed in Kunming mice (n = 6). 15 μL blood was collected at given time (2 min, 5 min, 10 min, 30 min, 1 h, 2 h, 4 h, 8 h and 24 h) after intravenous injection. Then, the blood sample was dispersed into 1 mL sterile saline with heparin sodium injection (50 unit mL^{-1}). The concentration of Ta was measured by ICP-AES. The *in vivo* blood terminal half-life of Ta_4C_3-IONP-SPs was determined by a double-component pharmacokinetic model.

In vitro and *in vivo* T_2-weighted MR imaging experiment

Before *in vitro* MR imaging, Ta_4C_3-IONP-SPs composite nanosheets with various iron concentrations (0-0.25 mM) were diluted with corresponding xanthan gum buffer solution (1 mg mL^{-1}) in Eppendorf tubes (2 mL volume) for MR test. T_2 map sequence is repetition time (TR) = 4000 ms; echo time (TE) = 13 ms; slice thickness = 2 mm; space = 0 mm; field of view (Fov) = 14; phase Fov = 0.75; freq × phase = 384 × 256; number excitations (Nex) = 2; echo train length (ETL) = 2. MR images were transferred to an ADW 4.6 workstation (GE Healthcare, Milwaukee, Wisc., USA). The mean T_2 values of each sample was determined by region-of-interest (ROI) using the T_2-mapping post-processing software on the MR unit, and the relaxation rate r_2 was calculated according to the reciprocal T_2 at various iron concentrations.

In vivo MRI evaluations was conducted on female BALB/c nude mice bearing 4T1 tumor allograft, which was established by subcutaneous injection of 1×10^7 4T1 tumor cells in PBS (200 μL) into the right hind limb of mouse. After the tumor growth for about two weeks, the Ta_4C_3-IONP-SPs composite nanosheets saline solution was injected into the mice (200 μL, 20 mg mL^{-1}) *via* tail vein. Mice were anaesthetized using 1% pentobarbital sodium (50 mg kg^{-1}) and the mice were placed in a prone position with a special animal imaging coil during the period of scanning. MR images were obtained at the given time intervals, and acquired in both coronal and axial orientations. The scan sequence was T_2-weighted Fast-recovery spin-echo (FR-FSE) with the parameters were described as follows: TR = 2800 ms; TE = 102.7 ms; slice thickness = 1.5 mm; space = 0.5 mm; FOV = 12; phase Fov = 0.75; freq × phase = 512 × 512; Nex = 2; ETL = 2.

In vitro and *in vivo* CT imaging experiment

For *in vitro* CT imaging, Ta_4C_3-IONP-SPs composite nanosheets with various Ta concentrations (1.25, 2.5, 5, 10 and 20 mg mL^{-1}) were dissolved in the Xanthan gum solution, and then were prepared in 1.5 mL micro-tubes. For comparison, the same concentrations of iopromide (Ultravist300, Bayer) were used as the control group. Imaging parameters were as follows: thickness = 1 mm; tube voltage = 120 kV; tube current = 92 mA; FOV = 86×86; gantry rotation time = 0.5 s; table speed = 6 mm s^{-1}.

For *in vivo* CT imaging, Ta_4C_3-IONP-SPs composite nanosheets (200 μL, 10 mg mL^{-1}) was intravenously administered into 4T1 tumor-bearing female BALB/c nude mice. CT images were acquired at different time intervals (3 min, 15 min, 30 min, 1 h, 2 h, and 2.5 h). Imaging parameters were as follows: thickness = 0.6 mm; tube voltage = 120 kV; tube current = 200 mA; FOV = 108×108; gantry rotation time = 0.75 s; table speed = 16.7 mm s^{-1}. Thin axial image was reformed to coronal images by computational technique.

Results and Discussion

Design, synthesis and characterization of Ta_4C_3-IONP composite nanosheets

Figure 1 illustrates the schematic procedure for fabricating Ta_4C_3-IONP-SPs and their multifunctionalities for simultaneous contrast-enhanced MRI/CT diagnostic imaging and photothermal hyperthermia of breast cancer. Typically, Ta_4C_3 nanosheets were synthesized by HF etching of their corresponding bulk MAX-phase Ta_4AlC_3 ceramics, which removed the middle Al layer to exfoliate the layer-structured ceramics. The following ultrasound treatment further reduced the aggregation of Ta_4C_3 nanosheets and planar sizes to satisfy the biomedical requirements (Figure 1). Superparamagnetic IONPs were *in-situ* grown onto the surface of Ta_4C_3 nanosheets to endow Ta_4C_3-IONPs composite nanosheets with superparamagnetic property for cancer-theranostic applications. The surface of as-exfoliated Ta_4C_3 nanosheets contains negatively charged oxygen-containing groups, absorbing the positively charged Fe^{2+} of $FeSO_4$, and then oxidizing the introduced Fe^{2+} into Fe^{3+} to form IONPs under the alkaline condition. This magnetic-functionalizing procedure is quite simple but highly efficient and reproducible. These introduced superparamagnetic IONPs on the surface of Ta_4C_3 MXenes could act as the contrast agents for T_2-weighted MR imaging. It is noted that Ta_4C_3-IONPs composite nanosheets were not stable in physiological environment and easily aggregated, therefore, soybean phospholipid (SP) was used for further surface modification (designated as Ta_4C_3-IONP-SPs) to enhance the stability in physiological medium and facilitate *in vivo* applications. Based on the high photothermal-conversion performance and high X-ray attenuation coefficient, these Ta_4C_3-IONP-SPs were further explored as the contrast agents for CT imaging and PTAs for photothermal breast-cancer ablation *via* the intravenous administration, easily transform within the blood vessel and subsequent accumulation into tumor by the typical enhanced permeability and retention (EPR) effect.

Transmission electron microscopy (TEM) image of Ta_4C_3 exhibits a typical sheet-like topology after HF etching and further continuous ultrasound treatment, which could render the resulting Ta_4C_3 nanosheets with small planar size and high dispersity (Figure 2A and B). High-resolution TEM (HRTEM) image and selected-area electron diffraction (SAED) pattern demonstrate the paralleled and ordered lattice fringes in the hexagonal symmetric lattice of Ta_4C_3 nanosheets, confirming that the exfoliation procedure did not significantly damage the planar structure of Ta_4C_3 nanosheets (Figure 2C and D). The HRTEM image of Ta_4C_3 nanosheets reveals the lattice spacing of 0.26 nm, which can be assigned to d-spacing in the (111) plane of Ta_4C_3. After *in-situ* growth of IONPs, the obviously anchored IONPs on the surface of Ta_4C_3 nanosheets were observed in TEM image (Figure 2E and F). Especially, the decorated IONPs exhibit high crystallity, contributing to the superparamagnetic property. The lattice fringes in the HRTEM show the IONPs (d-spacing 0.30 nm) decorated on the surface of Ta_4C_3 nanosheets (d-spacing 0.26 nm), whereas the d-spacing of 0.30 nm was indexed to the (400) plane of the Fe_3O_4

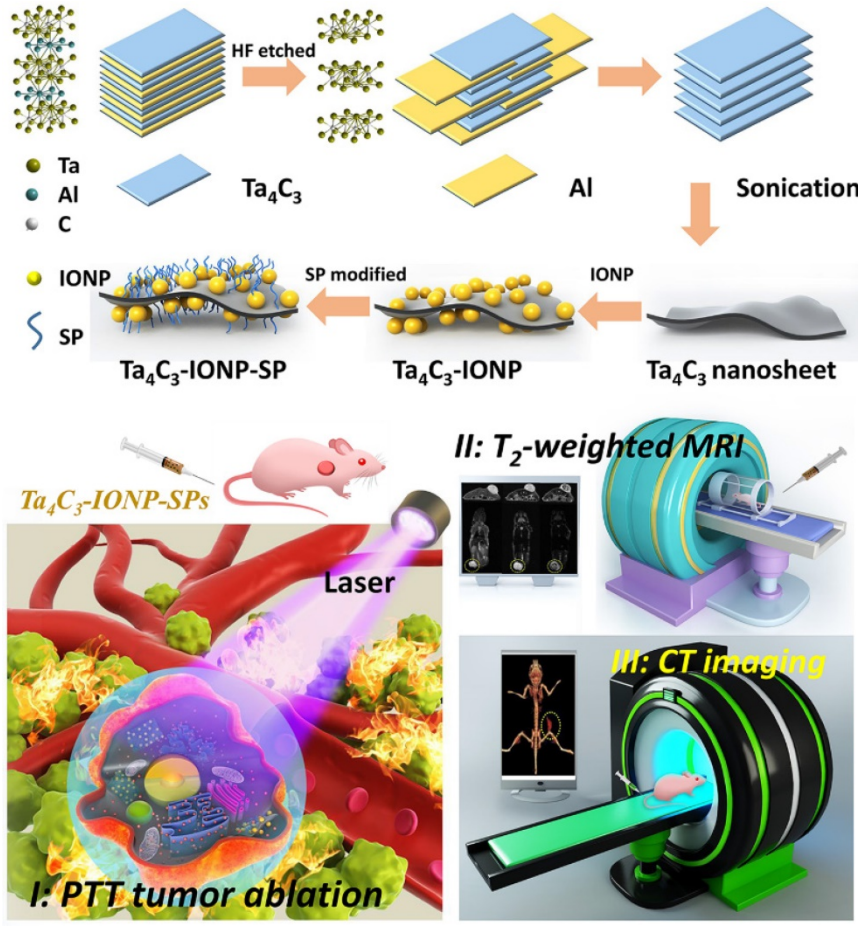

Figure 1. Schematic illustration of the fabrication process of Ta_4C_3-IONP-SPs composite nanosheets and their unique functionality for dual-modal contrast-enhanced MRI/CT imaging-guided photothermal ablation of breast cancer.

nanoparticles. (Figure 2G and H). The crystal of Ta_4C_3 nanosheets and Ta_4C_3-IONP composite nanosheets were characterized by X-ray diffraction (XRD, Figure 2I). The peaks at 2θ = 30.2° (220), 35.5° (311), 43.1° (400), 53.4° (422), 57.0° (511), 62.5° (440), 70.9° (620) and 73.9° (533) show the typical characteristics of Fe_3O_4 phase (JCPDS no. 19-0629) [40]. The characteristic peaks of Fe_3O_4 crystal phase demonstrated the formation of magnetic nanoparticles loaded onto Ta_4C_3 nanosheets. Although the pristine Ta_4C_3 nanosheets and the post-formed Ta_4C_3-IONP composite nanosheets have the similar main diffraction peaks in XRD patter, the Ta_4C_3-IONP composite nanosheets show the newly emerged 62.5° peak of IONPs, which could be indexed to (440) crystal facet of IONPs. X-ray energy dispersive spectroscopy (EDS) results confirm the presence of Ta, C, O, and Fe elements in Ta_4C_3-IONPs composite nanosheets (Figure 2J). Electron energy loss spectrum (EELS) also verifies the existence of corresponding elements, further confirming the successful decoration of IONPs onto the surface of MXene nanosheets (Figure 2K and L).

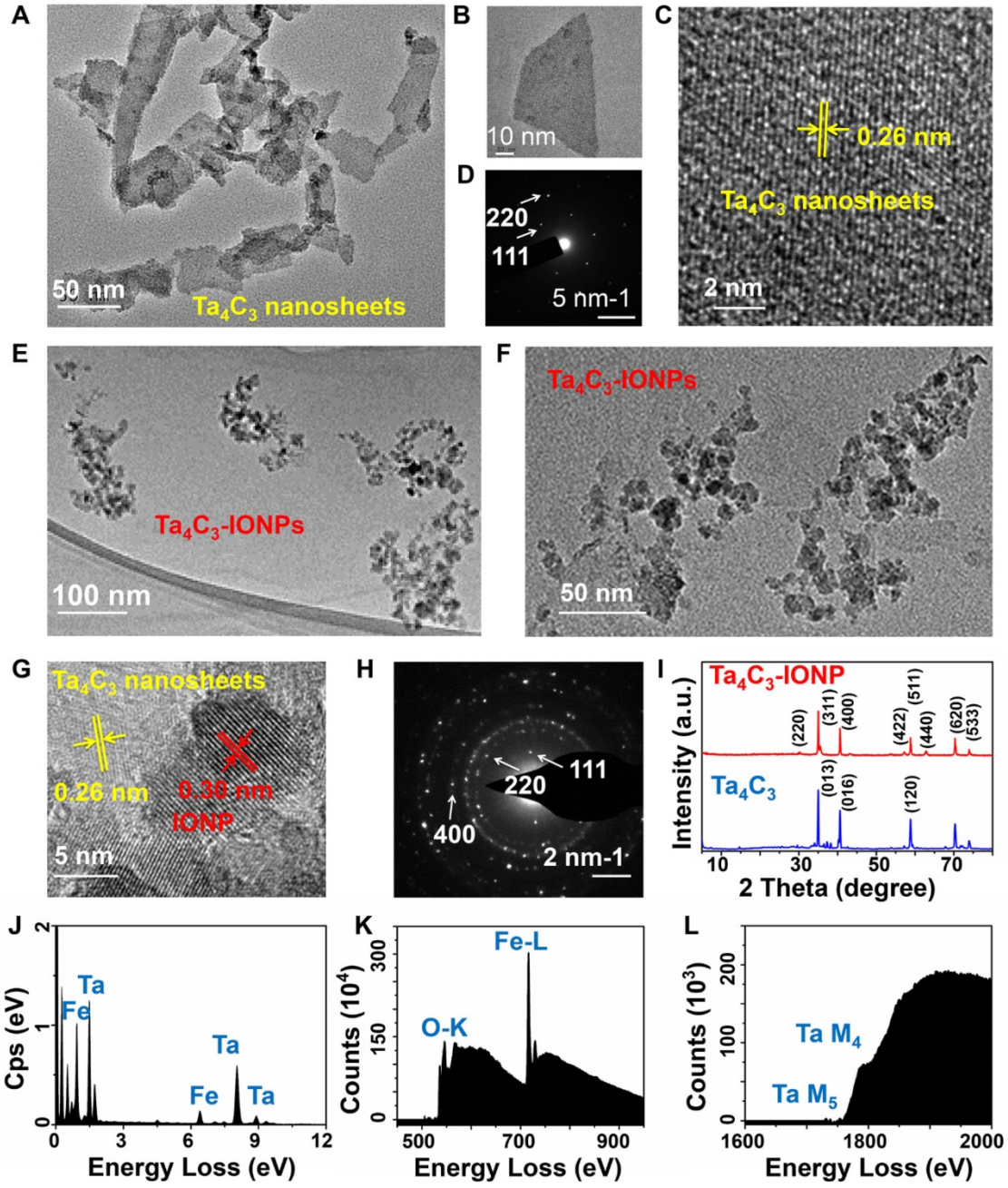

Figure 2. (A, B) TEM, (C) HRTEM and (D) SAED pattern images of as-synthesized 2D ultrathin Ta_4C_3 nanosheets. (E, F) TEM, (G) HRTEM and (H) SAED pattern images of multi-functionalized Ta_4C_3-IONP composite nanosheets. (I) X-ray diffraction (XRD) profiles of Ta_4C_3 nanosheets and Ta_4C_3-IONP composite MXenes. (J) EDS and (K, L) EELS of Ta_4C_3-IONP composite MXenes.

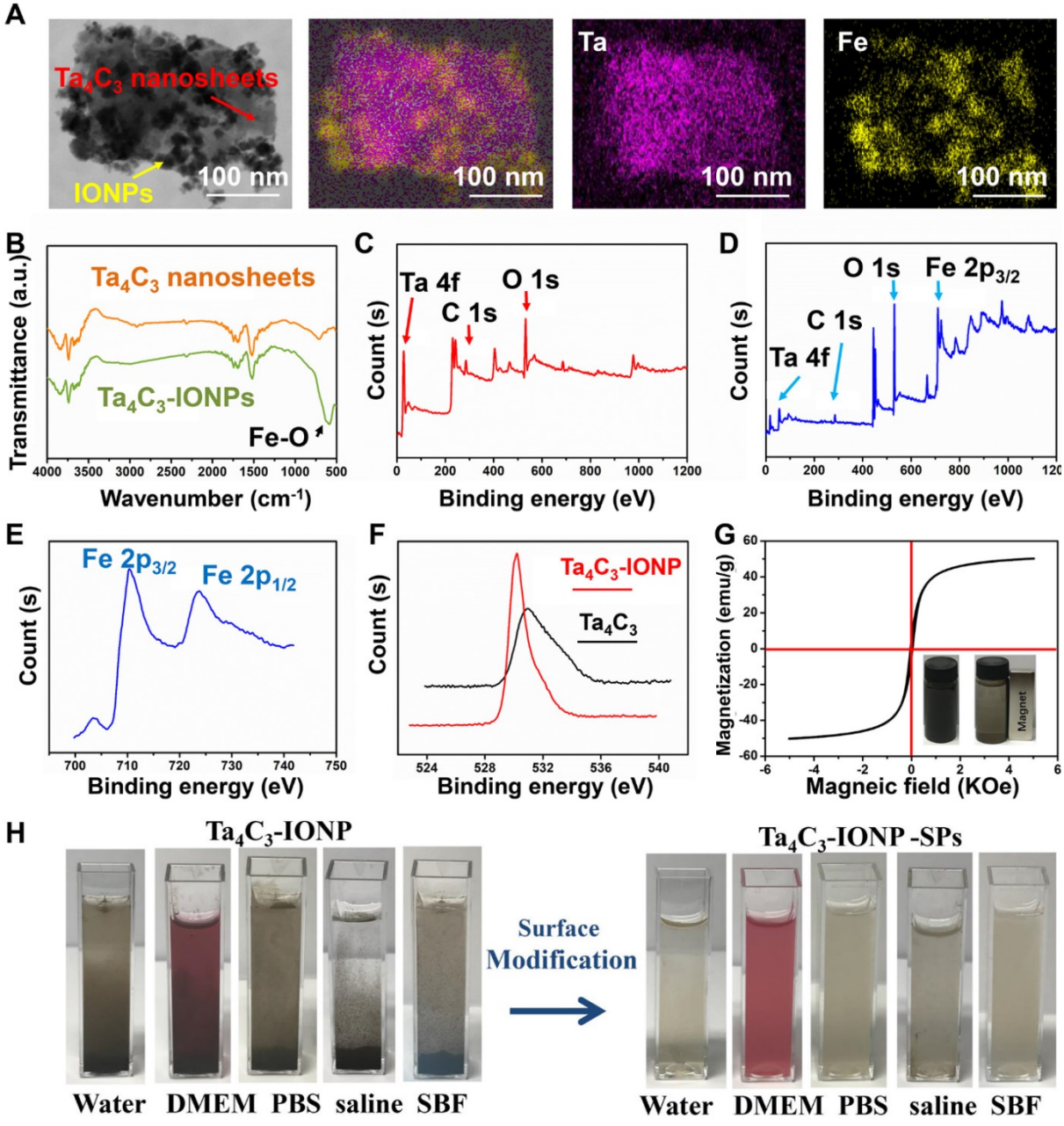

Figure 3. (A) STEM images of Ta_4C_3-IONP composite MXenes and corresponding element mapping images, showing the uniform distribution of Ta (purple) and Fe (yellow) elements in the whole matrix. (B) FTIR spectra of as-synthesized Ta_4C_3 nanosheets and Ta_4C_3-IONP composite nanosheets. XPS spectra of (C) Ta_4C_3 nanosheets and (D) Ta_4C_3-IONP composite nanosheets. Corresponding XPS spectra of (E) Fe 2p and (F) O 1s peaks of Ta_4C_3-IONP composite MXenes. (G) Magnetization curves of Ta_4C_3-IONP composite MXenes (Inset: a typical photographic image showing the facile magnetic separation of Ta_4C_3-IONP composite MXenes by an outer applied magnet). (H) Photographs of Ta_4C_3-IONP and Ta_4C_3-IONP-SPs composite nanosheets dispersed in various solutions (water, DMEM, PBS, saline and SBF).

Scanning transmission electron microscopy (STEM) images and corresponding element mapping directly display the uniform distribution of Ta and Fe element signals on the surface of Ta_4C_3-IONPs composite nanosheets (Figure 3A), indicating that the *in-situ* triggered redox reaction between Fe^{2+} and MXenes' surface could achieve the uniform magnetic functionalization of Ta_4C_3 nanosheets. The synthesis of Ta_4C_3-IONP composite MXenes was based on the typical reaction between Fe^{2+} and surface chemistry of carbon-based 2D materials [41]. With the interaction between superparamagnetic IONPs and oxygen-containing groups on the surface of Ta_4C_3 nanosheets, the band of Fourier Transform Infrared (FTIR) changes, which could be verified by a new peak at about 585 cm^{-1} in the FTIR spectrum of Ta_4C_3-IONP, due to the Fe-O vibration of Fe_3O_4, indicating the transform of Fe^{2+} to Fe^{3+} in the presence of

oxygen-containing groups of Ta_4C_3 nanosheets (Figure 3B). X-ray photoelectron spectroscopy (XPS) spectrum was also employed to confirm this redox reaction between Fe^{2+} and oxidizing surface of Ta_4C_3 nanosheets. Compared with the presence of tantalum, carbon and oxygen signals of Ta_4C_3 nanosheets in XPS spectrum (Figure 3C), the iron signals of Ta_4C_3-IONP is observed after the redox reaction (Figure 3D), demonstrating the successfully deposition of Fe_3O_4 onto the Ta_4C_3 nanosheets. The presence of Fe_3O_4 nanoparticle in Ta_4C_3-IONPs is also confirmed by high-resolution Fe 2p spectrum, in which the peaks at 710 and 724 eV are the characteristics of Fe $2p_{3/2}$ and Fe $2p_{1/2}$ of Fe_3O_4 (Figure 3E). The loss of oxygen-containing groups in Ta_4C_3 nanosheets after the surface redox reaction was certified by the high-resolution O 1s spectrum (Figure 3F). It has been found that the peaks at 530.4, 532.4, and 533.5 eV were assigned to TaC_x (-O terminated), $Ta_4C_3(OH)_x$ (-OH terminated), and $Ta_4C_3(OH)_x$-H_2O_{ads} (-OH terminated with strongly adsorbed water), respectively, which ensure that the oxygen-containing groups on the surface of Ta_4C_3 nanosheets were mainly -O and -OH, providing the target spots for *in-situ* growing IONPs (Figure S1).

Further evidence for the presence of magnetic Fe_3O_4 nanoparticles in Ta_4C_3-IONPs composite nanosheets comes from the magnetic modulation property. Ta_4C_3-IONPs composite nanosheets are capable of magnetic separation using an external bar magnet (Figure 3G), indicating the potential applications in further magnetic-field targeting theranostics. Absence of the hysteresis loop in the field-dependent magnetization verified the superparamagnetic feature of Ta_4C_3-IONPs MXenes. Especially, the saturation magnetization value of Ta_4C_3-IONPs composite nanosheets could reach 49.0 emu g^{-1} at room temperature, indicating their possible applications as T_2-MRI contrast agent (Figure 3G).

The as-prepared Ta_4C_3 nanosheets could be easily dispersed into aqueous condition but lack of relatively high stability, which were easily aggregated and precipitated in physiological solution. SP was adopted to modify the surface of Ta_4C_3-IONPs, by which the stability and dispersibility of Ta_4C_3-IONPs in various physiological media could be significantly improved, including water, Dulbecco's modified Eagle's medium (DMEM), phosphate buffer solution (PBS), saline solution and simulated body fluid (SBF) (Figure 3H). Because of the redox reaction-based surface magnetic functionalization and surface SP modification of Ta_4C_3 nanosheets, the average diameter of Ta_4C_3-IONP-SP (255.0 nm) is slightly larger than that of Ta_4C_3-IONP (190.1 nm) and Ta_4C_3 (141.8 nm) as determined by dynamic light scattering (DLS) (Figure S2). Ta_4C_3-IONP-SPs also show relatively high dispersity in different physiological solutions at varied time points (Figure S3). In addition, the negative zeta potentials of Ta_4C_3, Ta_4C_3-IONP and Ta_4C_3-IONP-SPs were measured to be-24.2 mV, -13.2 mV and -49.2 mV, respectively (Figure S4).

In vitro photothermal performance of Ta_4C_3-IONP-SP composite nanosheets

It is very intriguing that the as-synthesized Ta_4C_3 nanosheets intrinsically have high photothermal-conversion capability. Especially, the integration of IONPs onto the surface of Ta_4C_3 nanosheets was expected to keep the initial photothermal-conversion performance of Ta_4C_3 nanosheets. To verify this assumption, the *in vitro* photothermal-heating performance of Ta_4C_3-IONP-SPs was initially evaluated in aqueous solution. The photothermal-heating profiles of Ta_4C_3-IONP-SPs were recorded at different concentrations under 808 nm NIR laser irradiation at the power density of 1.5 W cm^{-2} (Figure 4A and B). Under NIR laser irradiation, the temperature of Ta_4C_3-IONP-SPs composite MXenes rose rapidly. Notably, at Ta_4C_3-IONP-SPs concentration of 200 ppm, the aqueous solution temperature could reach almost 46 °C within 10 min of NIR irradiation. Comparatively, the water temperature showed no obvious elevation at the same NIR irradiation condition, which demonstrated that Ta_4C_3-IONP-SPs could efficiently convert the NIR light energy into thermal energy. Furthemore, the photothermal-conversion stability of Ta_4C_3-IONP-SPs was confirmed by four laser on/off cycles where the temperature of Ta_4C_3-IONP-SPs aqueous solution did not exhibit obvious decline during these on/off circles, indicating that Ta_4C_3-IONP-SPs could act as the high-performance PTAs for continuous photothermal hyperthermia (Figure 4C). The temperature-steady state remains invariant with time extending. When the irradiation laser source was shut off, the temperature decrease was monitored to calculate the heat transfer rate from the aqueous solution to the environment (Figure 4D), which was used for the following evaluation on the photothermal-conversion efficacy of the composite nanosheets.

The ideal PTAs should not only possess strong extinction coefficient (ε), which represents the light-absorption performance, but also have high photothermal-conversion efficiency (η), which represents the capability of converting the light into heat energy [42]. The optical absorption spectra of Ta_4C_3-IONP-SPs did not show obvious NIR absorbance peaks at 808 nm with only a broaden

absorption tendency as compare to traditional Ti_3C_2 nanosheets [16]. However, the UV-vis-NIR spectra of as-synthesized Ta_4C_3-IONP-SPs at different concentrations exhibit a relatively good linear relationship between concentration and absorbance increase in the NIR range (808 nm, Figure 4E). To further reveal the NIR absorption capability of Ta_4C_3-IONP-SPs, the extinction coefficient (α) was calculated (see the *In vitro* photothermal performance of Ta_4C_3-IONP-SP composite nanosheets for the detailed calculations). The extinction coefficient of Ta_4C_3-IONP-SPs at 808 nm was determined to be 4.0 $Lg^{-1}\,cm^{-1}$ (inset of Figure 4E), which was higher than that of the mostly reported graphene oxide (GO) nanosheets (3.6 $Lg^{-1}\,cm^{-1}$) [42]. Based on the results of time constant for heat transfer and the maximum steady-state temperature, the photothermal-conversion efficiency (η) of Ta_4C_3-IONP-SPs was calculated to be as high as 32.5% (Figure 4D), much higher as compared to those of Au nanorods (21 %) [43], $Cu_{2-x}Se$ (22 %) [44], 2D MoS_2 (24.37 %) [45] and 2D black phosphorus (28.4 %) [46].

Based on the desriable extinction coefficient (ε) and high photothermal-conversion efficiency (η) of Ta_4C_3-IONP-SPs composite nanosheets, *in vitro* photothermal performance against breast-cancer cell lines (4T1 cell line) was initially evaluated (Figure 4F). Cell viability test was determined by the standard Cell-Counting Kit-8 (CCK-8) assay. Breast 4T1 cancer cells were incubated with Ta_4C_3-IONP-SPs at elevated concentrations (0, 12.5, 25, 50, 100, 200 ppm) for 24 h and no significant cytotoxicity was observed even at high Ta_4C_3-IONP-SPs concentration up to 200 ppm (Figure 4G). The photothermal efficiency of Ta_4C_3-IONP-SP composite nanosheets for cancer-cell ablation under NIR irradiation was further assessed. 4T1 cancer cells were incubated with Ta_4C_3-IONP-SPs at elevated concentrations (0, 12.5, 25, 50, 100, 200 ppm) for 4 h and then irradiated under 808 nm laser for 5 min at the power density of 1.5 W cm^{-2}. As expected, the photothermal-killing effect was observed with the increase of Ta_4C_3-IONP-SPs concentrations, where more cancer cells were ablated and then killed under the NIR irradiation (Figure 4H). Furthermore, confocal microscopic images of Calcein-AM and propidium iodide (PI) co-stained cancer cells also intuitively demonstrated the apoptosis of 4T1 cells because of the effective photothermal ablation induced by Ta_4C_3-IONP-SPs (Figure 4I). The majority of destructed cells after the treatment with Ta_4C_3-IONP-SPs under the NIR laser irradiation were clearly observed by the presence of strong red fluorescence (PI). In contrast, the viability of 4T1 cells incubated without Ta_4C_3-IONP-SPs or the only NIR laser irradiation was not obviously affected as displayed by a strong green fluorescence (Calcein-AM). Confocal laser scanning microscopy (CLSM) images clearly show the efficient intracellular uptake of FITC (fluorescein isothiocyanate)-labeled Ta_4C_3-IONP-SPs after the co-incubation for different durations (1, 2, 4 and 6 h; Figure S5).

Contrast-enhanced diagnostic MRI/CT imaging assisted by Ta_4C_3-IONP-SP composite nanosheets

The superparamagnetic Fe_3O_4 nanoparticles have been extensively explored as the efficient contrast agents for T_2-weighted MR imaging [47]. To explore the possibility of using superparamagentic Ta_4C_3-IONP-SPs composite nanosheets in enhanced MR imaging, the T_2 relaxation time was meatured under elevated concentrations. An obvious concentration-dependent and contrast-enhanced negative T_2-weighted MR images were recorded (Figure 5A). The T_2 relaxivity (r_2) of Ta_4C_3-IONP-SPs was calculated to be as high as 205.46 $mM^{-2}s^{-1}$, much higher as compared to commercial T_2 contrast agents (72.0 $mM^{-2}s^{-1}$ of ferumoxsil and 98.3 $mM^{-2}s^{-1}$ of ferumoxide) [48] because of the unique superparamagneitc property, high magneitc saturaztion value and magnetic aggregation-enhanced MRI performance of Ta_4C_3-IONP-SPs composite nanosheets. Based on the high transverse relaxivity, Ta_4C_3-IONP-SPs as contrast agents of T_2-weighted MR imaging was further evaluated *in vivo* on 4T1 tumor-bearing mice allograft. Regions of hypointense signal T_2 images was found in tumor sites, which became more obvious along with the observation time window (Figure 5B). The changes of quantitative T_2 negative signal values in tumor tissue (Figure 5C) further verified the contrast-enhanced T_2-weighted MR imaging capability of Ta_4C_3-IONP-SPs. Based on above results, it is expected that these superparamagnetic Ta_4C_3-IONP-SPs composite MXenes could provide a non-invasive method for further diagnostic imaging-guided photothermal hyperthermia of breast cancer or monitoring the therapeutic process during photothermal ablation.

In addition to the MR imaging technique, CT imaging is also one of important medical imaging modalities in clinical practice. Ta_4C_3-IONP-SPs were further developed as CT contrast agents based on the high atomic number of Ta compomnent, which could provide remarkably increased contrast. To further assess the feasibility of Ta_4C_3-IONP-SPs composite nanoparticles as contrast agents in the CT imaging, Ta_4C_3-IONP-SPs were dispersed in aqueous solution at various concentrations. An obviously linear relationship between the enhanced CT value (HU) and the increased Ta_4C_3-IONP-SPs concentrations was

observed (Figure 6A and B). Especially, at the same concentration, the CT value of Ta_4C_3-IONP-SPs was much higher than that of a commercial iodine-based contrast agents (iopromide). Encouraged by the high *in vitro* CT value, Ta_4C_3-IONP-SPs as novel CT contrast agents was evaluated *in vivo* on 4T1-bearing breast-cancer nude mice allograft. A significant attenuation on CT images in the tumor sites was observed after intravenous injection of Ta_4C_3-IONP-SPs. Consistent to transverse and coronal section images, 3D-rendering axial images also illustrated marked contrast enhancement in tumor after tail-vein injection of Ta_4C_3-IONP-SPs (Figure 6C). The gradual increase of CT values (Figure 6D) in tumor further verified the accumulation of Ta_4C_3-IONP-SPs into tumor and corresponding contrast-enhanced CT imaging, indicating the potential of Ta_4C_3-IONP-SPs as CT contrast probes for diagnostic imaging of breast tumor.

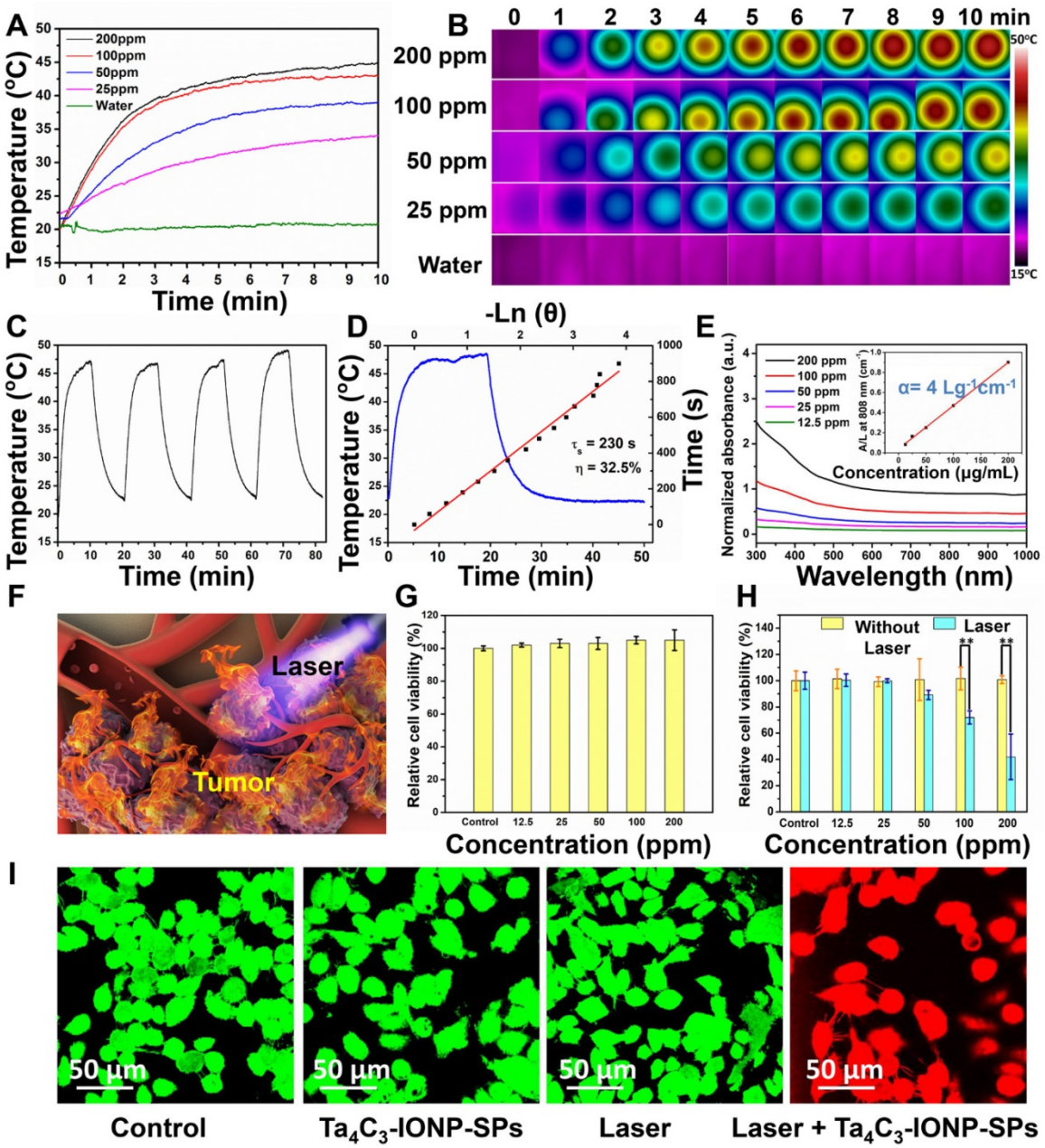

Figure 4. (A) Photothermal-responding profiles of Ta_4C_3-IONP-SPs under laser irradiation (808 nm, 1.5 W cm^{-2}) for 10 min at elevated concentrations, and (B) the corresponding infrared thermal images. (C) Heating/cooling profiles of Ta_4C_3-IONP-SPs dispersed in deionized water (200 ppm) for four cycles of laser irradiation (808 nm, 1.5 W cm^{-2}). (D) Temperature-changing profile of Ta_4C_3-IONP-SPs (200 ppm) under 808 nm laser at 1.5 W cm^{-2} until reaching the temperature-steady state. (E) UV-vis spectra of Ta_4C_3-IONP-SPs at various concentrations (12.5, 25, 50, 100, 200 ppm). Inset: normalized absorbance intensity at λ = 808 nm. (F) 3D-schematic illustration of Ta_4C_3-IONP-SPs as PTAs for 4T1 cell ablation under the exposure to 808 nm laser irradiation. (G) Relative viabilities of 4T1 cells after incubation with Ta_4C_3-IONP-SPs at elevated concentrations for 24 h. (H) Relative viabilities of 4T1 cells after incubation with Ta_4C_3-IONP-SPs with or without laser irradiation (808 nm, 1.5 W cm^{-2}, 10 min). **significant difference at $P < 0.01$. (I) Confocal fluorescence images of calcein AM (green, live cells) and propidium iodide (red, cells) co-stained cells after the incubation with Ta_4C_3-IONP-SPs under different treatments.

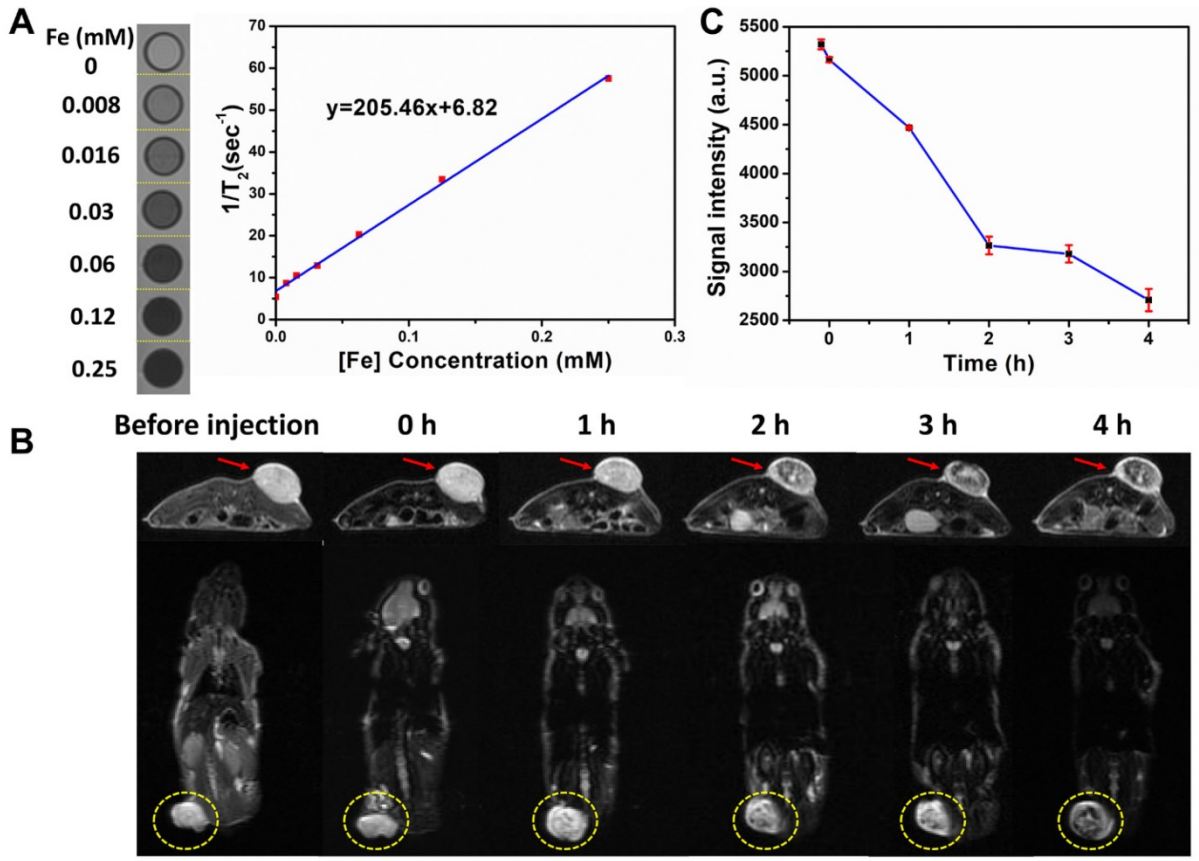

Figure 5. (A) *In vitro* T_2-weighted MR imaging and T_2 relaxivity of Ta_4C_3-IONP-SPs composite MXenes. (B) Transverse and coronal section of T_2-weighted MR imaging of 4T1 tumor-bearing mouse before and after intravenous injection of Ta_4C_3-IONP-SPs at given time points, and (C) the corresponding T_2-weighted MRI signal intensities of tumor site at varied time points after the intravenous administration of Ta_4C_3-IONP-SPs composite MXenes. The tumor sites were marked by red arrows and yellow circles.

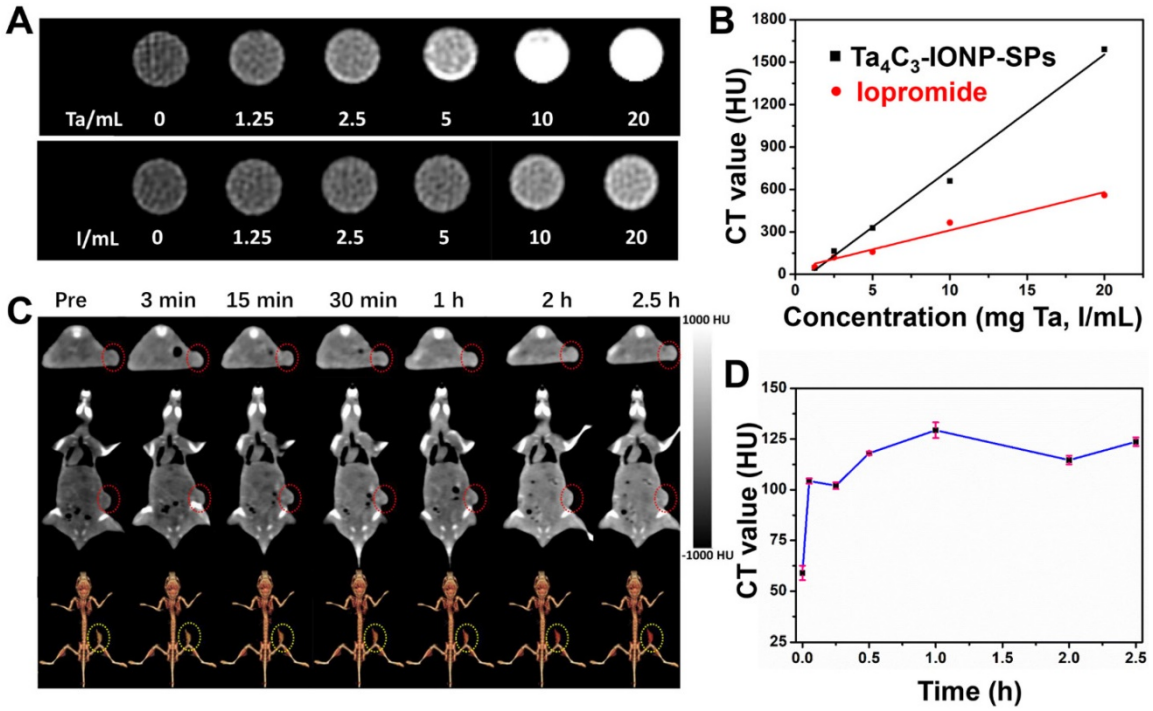

Figure 6. *In vitro* (A) CT images and (B) the corresponding CT values (HU) of Ta_4C_3-IONP-SPs composite MXenes and iopromide solutions at varied concentrations. (C) Transverse, coronal and 3D-rendering CT images of 4T1 tumor-bearing mouse before and after intravenous injection of Ta_4C_3-IONP-SPs, and (D) time-dependent corresponding CT values of tumor site after the intravenous administration of Ta_4C_3-IONP-SPs composite MXenes. The tumor sites were marked by red circles.

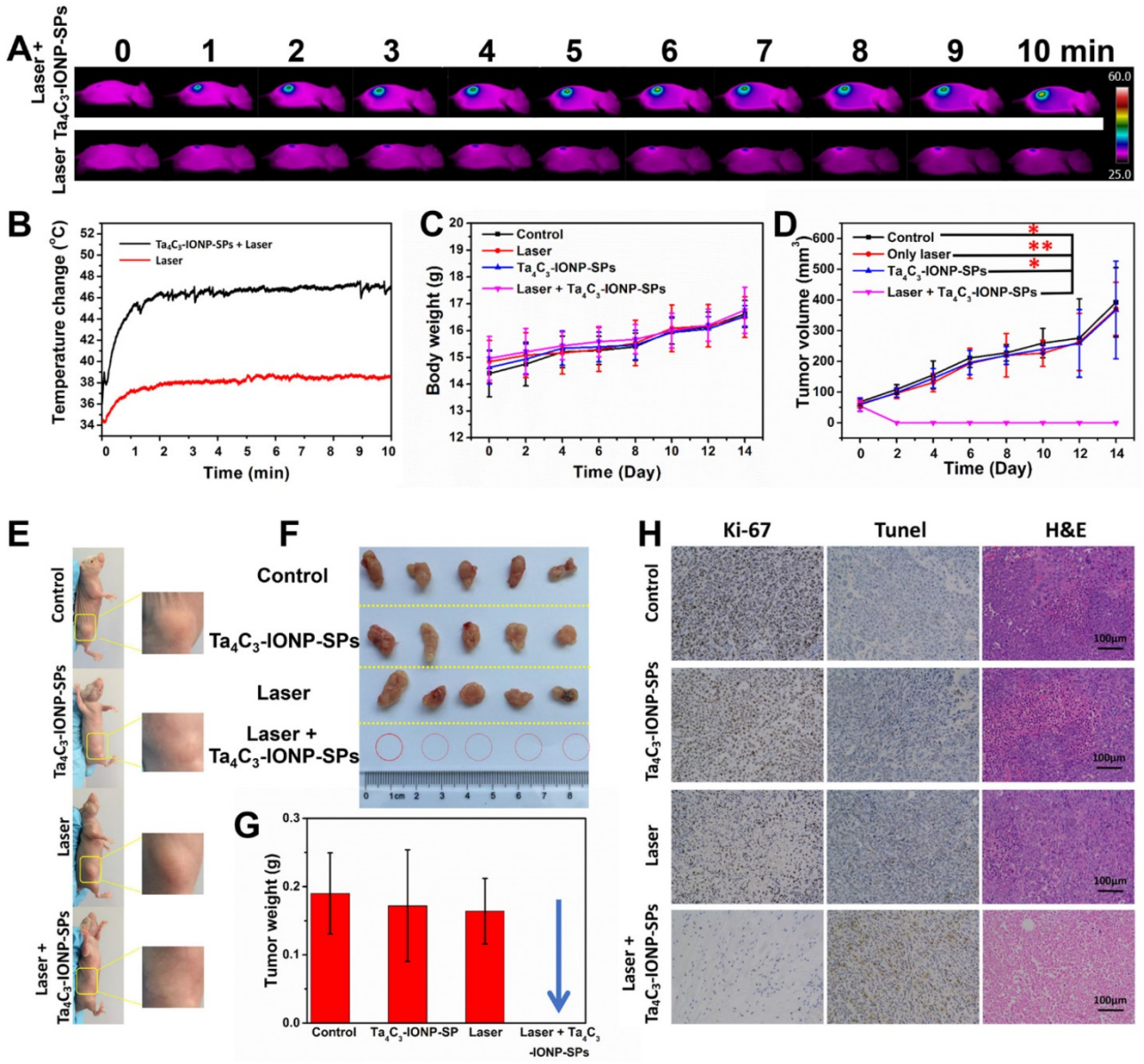

Figure 7. (A) *In vivo* IR images of 4T1 tumor-bearing mice before and after intravenous injection of Ta_4C_3-IONP-SPs MXenes under the exposure to laser irradiation (808 nm, 1.5 W cm^{-2}, 10 min), and (B) the corresponding temperature elevation of tumor sites during the period of laser irradiation. (C) Time-dependent body-weight changing profiles and (D) tumor-volume changing curves of four groups of 4T1 tumor-bearing mice after different treatments. *significant difference at $P < 0.05$. **significant difference at $P < 0.01$. (E) Photographs of 4T1 tumor-bearing mice at the 14th day after various treatments, (F) corresponding photographs, and (G) tumor weight of 4T1 tumors collected from all groups after varied treatments. (H) Antigen Ki-67 immunofluorescence, Tunel and H&E stained histological sections of tumor tissues from the mice after PTT treatment in each group (scale bar, 100 μm).

In vivo photothermal breast-cancer hyperthermia assisted by Ta_4C_3-IONP-SP composite nanosheets

Inspired by the desirable *in vitro* PTT performance, the therapeutic efficacy of Ta_4C_3-IONP-SPs MXene *in vivo* was conducted on 4T1 tumor-bearing mice. Once the average tumor volume reached about 50 mm^3, the tumor-bearing mice were randomized into four groups: (i) intravenous administration of PBS taken as control group, (ii) intravenous administration of PBS and irradiated by 808 nm-laser at the power density of 1.5 W cm^{-2} for 10 min taken as laser only group, (iii) intravenous administration of Ta_4C_3-IONP-SPs (20 mg mL^{-1}) taken as Ta_4C_3-IONP-SPs only group, and (vi) intravenous administration of Ta_4C_3-IONP-SPs (20 mg mL^{-1}) and irradiated by 808 nm-laser at the power density of 1.5 W cm^{-2} for 10 min taken as laser irradiation post-injection of Ta_4C_3-IONP-SPs group. The surface temperature and corresponding thermal images of the irradiated mice were recorded by an infrared thermal imaging instrument (Figure 7A and B). IR thermal images uncover the rapid rise of surface temperature in the tumor of mice after intravenous injection with Ta_4C_3-IONP-SPs upon NIR laser irradiation, whereas

in PBS-injected mice under the same NIR irradiation condition only show slight temperature change. The temperature of the tumors from mice in post-injection of Ta_4C_3-IONP-SPs increases from about 34 °C to 48 °C within 10 min, which is sufficiently high to ablate cancer cells and tumor tissues. As shown in Figure S6, two days after photothermal hyperthermia, the initial tumors disappeared in group of injected with Ta_4C_3-IONP-SPs under laser irradiation, leaving black scars at tumor sites. The body-weight and tumor volumes of all groups were measured every two days (Figure 7C and D), and the digital photos of tumor area were taken at the same time (Figure S6). Importantly, during the experimental period of half a mouth after different treatments, tumors in groups of Ta_4C_3-IONP-SPs with irradiation were completely eradicated without reoccurrence, whereas tumors in other three groups continued to grow until the end of the experiment (Figure 7E-G). Biodistribution of Ta_4C_3-IONP-SPs in main organs and tumor was measured on 4T1 tumor-bearing nude mice at 24 h post *i.v.* injection. It was found that around 1.02% Ta_4C_3-IONP-SPs could accumulate in the tumor tissue passively due to the EPR effect (Figure S7). Retention of Ta_4C_3-IONP-SPs in liver and spleen may be attributed to the abundant macrophage uptake of nanoparticles in reticuloendothelial systems. In addition, Ta_4C_3-IONP-SPs could be excreted out of the body via the feces and urines with the prolonged feeding time (Figure S8).

Antigen Ki-67 immunofluorescence, terminal deoxynucleotidyl transferase-mediated dUTP nick end labeling (TUNEL) and hematoxylin and eosin (H&E) staining images of tumor sections were further used to evidence the high PTT efficacy of Ta_4C_3-IONP-SPs upon laser irradiation (Figure 7H). The histopathological analysis of the tumor specimens in the group of control, laser only and Ta_4C_3-IONP-SPs only shows no obvious differences including the cell-shape, nuclear morphology or necrosis. It suggests that only 808 nm laser irradiation or only Ta_4C_3-IONP-SPs is not effective in killing the cancer cells. In the group of Ta_4C_3-IONP-SPs combined with NIR laser irradiation, thermal-related cell necrosis is presented on most regions of tumor site, as well as other particular cell necrosis feature, such as cells shrunken, nuclei pyknotic and fragmentized. In addition, proliferative and apoptosis activities are also observed in Ki-67 antibody and TUNEL staining, which confirmed the remarkable photothermal effect of the Ta_4C_3-IONP-SPs for *in vivo* cancer-cell ablation.

In vivo biocompatibility assay of Ta_4C_3-IONP-SP composite nanosheets

To further guarantee the potential clinical translation, the *in vivo* biocompatibility of Ta_4C_3-IONP-SPs composite nanosheets was investigated on healthy Kunming mice, which were divided into four groups at random, including control group and three treatment groups at three doses (5, 10, and 20 mg kg^{-1}). After intravenous administration of Ta_4C_3-IONP-SPs for each treatment groups, the mice were then fed for one month. All mice behaved normally without any obvious body-weight loss or accidental death (Figure S9). The blood indexes, including liver and kidney function indexes, red blood cells (RBC), white blood cells (WBC), platelets (PLT), lymphocytes (LYM), mean corpuscular hemoglobin (MCH), mean corpuscular hemoglobin concentration (MCHC), mean corpuscular volume (MCV), hemoglobin (Hb), and hematocrit (HCT) exhibit no obvious hepatic and kidney toxicity among the control group and the treatment groups (Figure 8A-L). The H&E staining sections of main organs (heart, liver, spleen, lung, and kidney) of mice in the experimental groups after one-month feeding show no significant damage or acute inflammation as compared to the control group (Figure 8M). The blood circulation half-time of Ta_4C_3-IONP-SPs was calculated to be 0.5 h (Figure S10). These preliminary biocompatibilty evaluation data demonstrate that Ta_4C_3-IONP-SPs composite nanosheets is biocompatible with low cytotoxicity for potential saft clinical translation, especially for further *in vivo* dual-mode MR/CT diagnsotic imaging-guided phothermal hyperthermia and ablation of breast tumor.

Conclusions

In summary, we have successfully constructed a novel superparamagnetic MXene-based theranostic nanoplatform for efficient breast-cancer theranostic, which was based on tantalum carbide (Ta_4C_3) MXene and its further surface superparamagnetic functionalization (Ta_4C_3-IONP-SPs composite MXenes). A unique surface reaction was triggered to *in-situ* grow magnetic iron oxide nanoparticles onto the surface of Ta_4C_3 MXene towards magnetic functionalization. These Ta_4C_3-IONP-SPs composite nanosheets have been demonstrated to exert three specific functionalities for breast-cancer theranostics. The Ta component was employed for contrast-enhanced CT imaging, and the integrated superparamagnetic IONPs acted as the contrast agents for T_2-weighted MR imaging. Especially, the high photothermal-conversion efficiency of Ta_4C_3-IONP-SPs composite nanosheets (η: 32.5%) has achieved complete tumor eradication without reoccurrence, demonstrating the highly efficient breast-tumor hyperthermia performance. The high biocompatibility has been preliminarily

demonstrated to guarantee the potential clinical translation of Ta_4C_3-IONP-SPs composite nanosheets. This work paves a new way for significantly broadening the biomedical applications of MXene-based nanoplatforms by exploring their novel family members (Ta_4C_3 MXene in this work) and their further functionalization strategies (magnetic functionalization in this work).

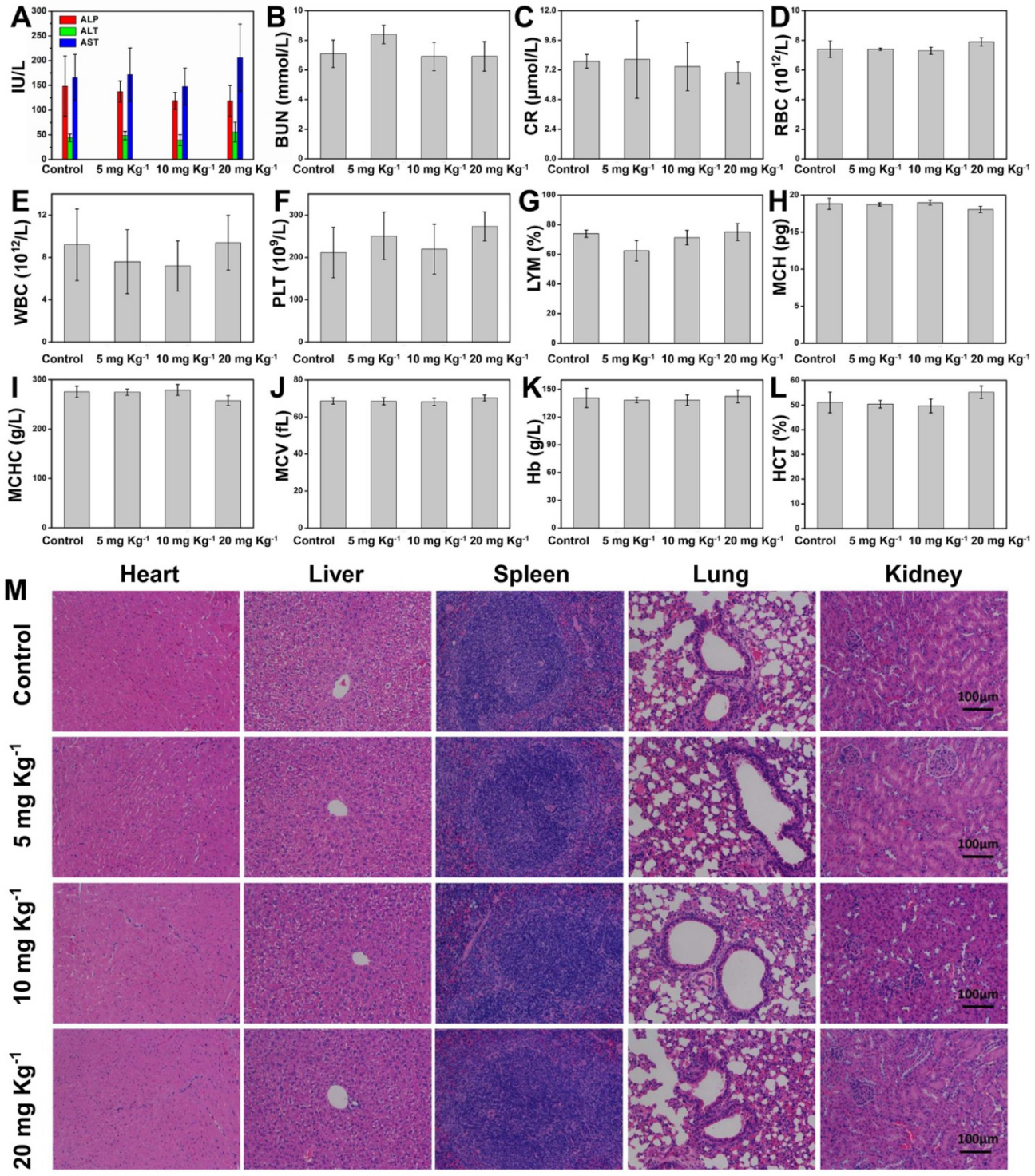

Figure 8. (A-L) Hematological test of Kunming mice from the control group and three treatment groups at 30th days after intravenous injection of Ta_4C_3-IONP-SPs at elevated doses (0, 5, 10 and 20 mg kg^{-1}). (M) H&E staining tissue sections of main organs including heart, liver, spleen, lung and kidney of Kunming mice after single intravenous injection of Ta_4C_3-IONP-SPs (0, 5, 10 and 20 mg kg^{-1}) for 30 days feeding. All the scale bars are 100 μm.

Abbreviations

CCK-8: Cell-Counting Kit-8; CLSM: confocal laser scanning microscopy; CT: X-ray computed tomography; DLS: dynamic light scattering; DMEM: Dulbecco's modified Eagle's medium; EDS: X-ray energy dispersive spectroscopy; EELS: electron energy loss spectrum; EPR: enhanced permeability and retention; ETL: echo train length; FBS: fetal bovine serum; Fov: field of view; FR-FSE: Fast-recovery spin-echo; FTIR: fourier transform infrared; Hb: hemoglobin; HCT: hematocrit; HF: hydrofluoric acid; HRTEM: high-resolution transmission electron microscopy; HU: hounsfield unit; H&E: hematoxylin and eosin; IACUC: Institutional Animal Care and Use Committee; ICP-AES: inductively coupled plasma atomic emission spectrometer; IONPs: iron oxide nanoparticles; IR: infrared; LYM: lymphocytes; MCH: mean corpuscular hemoglobin; MCHC: mean corpuscular hemoglobin concentration; MCV: mean corpuscular volume; MRI: magnetic resonance imaging; Nex: number excitation; NIR: near infrared; PBS: phosphate buffer solution; PI: propidium iodide; PLT: platelets; PTA: photothermal agent; PTT: photothermal therapy; RBC: red blood cells; ROI: region-of-interest; SAED: selected-area electron diffraction; SBF: simulated body fluid; SP: soybean phospholipid; SPF: specific pathogen-free; STEM: scanning transmission electron microscopy; TE: echo time; TEM: transmission electron microscopy; TR: repetition time; TUNEL: terminal deoxynucleotidyl transferase-mediated dUTP nick end labeling; WBC: white blood cells; XPS: X-ray photoelectron spectroscopy; XRD: X-ray diffraction; 2D: two-dimensional.

Acknowledgements

We greatly acknowledge the financial support from the National Key R&D Program of China (Grant No. 2016YFA0203700), National Natural Science Foundation of China (Grant No. 51722211 and 51672303), Natural Science Foundation of Shanghai (15ZR1407700) and Young Elite Scientist Sponsorship Program by CAST (Grant No. 2015QNRC001).

Supplementary Material

Supplementary figures.
http://www.thno.org/v08p1648s1.pdf

Competing Interests

The authors have declared that no competing interest exists.

References

1. Siegel RL, Miller KD, Jemal A. Cancer statistics, 2016. CA Cancer J Clin. 2016; 66: 7-30.
2. Greenlee H, DuPont-Reyes MJ, Balneaves LG, et al. Clinical practice guidelines on the evidence-based use of integrative therapies during and after breast cancer treatment. CA Cancer J Clin. 2017; 67: 194-232.
3. Kim EJ, Kang BJ, Kim SH, et al. Diagnostic Performance of and Breast Tissue Changes at Early Breast MR Imaging Surveillance in Women after Breast Conservation Therapy. Radiology. 2017; 3: 656-666.
4. Willmann JK, Van Bruggen N, Dinkelborg LM, et al. Molecular imaging in drug development. Nat Rev Drug Discov. 2008; 7: 591-607.
5. Novoselov KS, Jiang D, Schedin F, et al. Two-dimensional atomic crystals. Proc Natl Acad Sci U S A. 2005; 102: 10451-10453.
6. Geim AK, Novoselov KS. The rise of graphene. Nat Mater. 2007; 6: 183-191.
7. Li XL, Wang XR, Zhang L, et al. Chemically derived, ultrasmooth graphene nanoribbon semiconductors. Science. 2008; 319: 1229-1232.
8. Chen Y, Tan CL, Zhang H, et al. Two-dimensional graphene analogues for biomedical applications. Chem Soc Rev. 2015; 44: 2681-2701.
9. Chen Y, Wang LZ, Shi JL. Two-dimensional non-carbonaceous materials-enabled efficient photothermal cancer therapy. Nano Today. 2016; 11: 292-308.
10. Feng LY, Wu L, Qu XG. New horizons for diagnostics and therapeutic applications of graphene and graphene oxide. Adv Mater. 2013; 25: 168-186.
11. Chung C, Kim Y-K, Shin D, et al. Biomedical applications of graphene and graphene oxide. Acc Chem Res. 2013; 46: 2211-2224.
12. Chen WS, Ouyang J, Liu H, et al. Black Phosphorus Nanosheet-Based Drug Delivery System for Synergistic Photodynamic/Photothermal/Chemotherapy of Cancer. Adv Mater. 2017; 29: 1603864-1603871.
13. Cheng L, Liu JJ, Gu X, et al. PEGylated WS_2 nanosheets as a multifunctional theranostic agent for in vivo dual-modal CT/photoacoustic imaging guided photothermal therapy. Adv Mater. 2014; 26: 1886-1893.
14. Liu T, Wang C, Gu X, et al. Drug delivery with PEGylated MoS_2 nano-sheets for combined photothermal and chemotherapy of cancer. Adv Mater. 2014; 26: 3433-3440.
15. Chen Q, Feng LZ, Liu JJ, et al. Intelligent Albumin–MnO_2 Nanoparticles as pH-/H_2O_2-Responsive Dissociable Nanocarriers to Modulate Tumor Hypoxia for Effective Combination Therapy. Adv Mater. 2016; 28: 7129-7136.
16. Lin H, Wang XG, Yu LD, et al. Two-dimensional ultrathin MXene ceramic nanosheets for photothermal conversion. Nano Lett. 2016; 17: 384-391.
17. Xuan JN, Wang ZQ, Chen YY, et al. Organic-Base-Driven Intercalation and Delamination for the Production of Functionalized Titanium Carbide Nanosheets with Superior Photothermal Therapeutic Performance. Angew Chem Int Ed Engl. 2016; 128: 14789-14794.
18. Chen YY, Cheng L, Dong ZL, et al. Degradable Vanadium Disulfide Nanostructures with Unique Optical and Magnetic Functions for Cancer Theranostics. Angew Chem Int Ed Engl. 2017; 129: 13171-13176.
19. Yu J, Yin WY, Zheng XP, et al. Smart MoS_2/Fe_3O_4 Nanotheranostic for Magnetically Targeted Photothermal Therapy Guided by Magnetic Resonance/Photoacoustic Imaging. Theranostics. 2015; 5: 931-945.
20. Naguib M, Kurtoglu M, Presser V, et al. Two-dimensional nanocrystals produced by exfoliation of Ti_3AlC_2. Adv Mater. 2011; 23: 4248-4253.
21. Naguib M, Mashtalir O, Carle J, et al. Two-dimensional transition metal carbides. ACS Nano. 2012; 6: 1322-1331.
22. Mashtalir O, Naguib M, Mochalin VN, et al. Intercalation and delamination of layered carbides and carbonitrides. Nat Commun. 2013; 4: 1716.
23. Ghidiu M, Lukatskaya MR, Zhao MQ, et al. Conductive two-dimensional titanium carbide 'clay' with high volumetric capacitance. Nature. 2014; 516: 78-81.
24. Anasori B, Lukatskaya MR, Gogotsi Y. 2D metal carbides and nitrides (MXenes) for energy storage. Nat Rev Mater. 2017; 2: 16098.
25. Naguib M, Mochalin VN, Barsoum MW, Gogotsi Y. 25th anniversary article: MXenes: a new family of two-dimensional materials. Adv Mater. 2014; 26: 992-1005.
26. Xue Q, Zhang HJ, Zhu MS, et al. Photoluminescent Ti_3C_2 MXene Quantum Dots for Multicolor Cellular Imaging. Adv Mater. 2017; 29: 1604847.
27. Xu BZ, Zhu MS, Zhang WC, et al. Ultrathin MXene-Micropattern-Based Field-Effect Transistor for Probing Neural Activity. Adv Mater. 2016; 28: 3333-3339.
28. Rasool K, Helal M, Ali A, et al. Antibacterial Activity of $Ti_3C_2T_x$ MXene. ACS Nano. 2016; 10: 3674-3684.
29. Cheng L, Wang C, Feng LZ, et al. Functional nanomaterials for phototherapies of cancer. Chem Rev. 2014; 114: 10869-10939.
30. Yang K, Hu LL, Ma XX, et al. Multimodal imaging guided photothermal therapy using functionalized graphene nanosheets anchored with magnetic nanoparticles. Adv Mater. 2012; 24: 1868-1872.
31. Chou SS, Kaehr B, Kim J, et al. Chemically exfoliated MoS_2 as near-infrared photothermal agents. Angew Chem Int Ed Engl. 2013; 125: 4254-4258.
32. Jin RC, Cao YC, Hao E, et al. Controlling anisotropic nanoparticle growth through plasmon excitation. Nature. 2003; 425: 487-490.
33. Li RY, Zhang LB, Shi L, et al. MXene Ti_3C_2: an Effective 2D Light-to-Heat Conversion Material. ACS Nano. 2017; 11: 3752-3759.
34. Lee N, Cho HR, Oh MH, et al. Multifunctional Fe_3O_4/TaO_x Core/Shell Nanoparticles for Simultaneous Magnetic Resonance Imaging and X-ray Computed Tomography. J Am Chem Soc. 2012; 134: 10309-10312.

35. Lee N, Choi SH, Hyeon T. Nano-sized CT contrast agents. Adv Mater. 2013; 25: 2641-2660.
36. Pan XC, Siewerdsen J, La Riviere PJ, et al. Anniversary Paper: Development of x-ray computed tomography: The role of Medical Physics and AAPM from the 1970s to present. Med Phys. 2008; 35: 3728-3739.
37. Bonitatibus PJ, Jr., Torres AS, Goddard GD, et al. Synthesis, characterization, and computed tomography imaging of a tantalum oxide nanoparticle imaging agent. Chem Commun. 2010; 46: 8956-8958.
38. Chen HL, Liu ZM, Li SY, et al. Fabrication of Graphene and AuNP Core Polyaniline Shell Composite nanosheets as Multifunctional Theranostic Platforms for SERS Real-time Monitoring and Chemo-photothermal Therapy. Theranostics. 2016; 6: 1096-1104.
39. Roper DK, Ahn W, Hoepfner M. Microscale heat transfer transduced by surface plasmon resonant gold nanoparticles. J Phys Chem C. 2007; 111: 3636-3641.
40. Zeng T, Zhang XL, Ma YR, et al. A novel Fe_3O_4–graphene–Au multifunctional nanocomposite: green synthesis and catalytic application. J Mater Chem. 2012; 22: 18658-18663.
41. Xue YH, Chen H, Yu DS, et al. Oxidizing metal ions with graphene oxide: the in situ formation of magnetic nanoparticles on self-reduced graphene sheets for multifunctional applications. Chem Commun. 2011; 47: 11689-11691.
42. Robinson JT, Tabakman SM, Liang YY, et al. Ultrasmall reduced graphene oxide with high near-infrared absorbance for photothermal therapy. J Am Chem Soc. 2011; 133: 6825-6831.
43. Zeng J, Goldfeld D, Xia YN. A Plasmon-Assisted Optofluidic (PAOF) System for Measuring the Photothermal Conversion Efficiencies of Gold Nanostructures and Controlling an Electrical Switch. Angew Chem Int Ed Engl. 2013; 52: 4169-4173.
44. Hessel CM, Pattani VP, Rasch M, et al. Copper selenide nanocrystals for photothermal therapy. Nano Lett. 2011; 11: 2560-2566.
45. Yin WY, Yan L, Yu J, et al. High-Throughput Synthesis of Single-Layer MoS_2 Nanosheets as a Near-Infrared Photothermal-Triggered Drug Delivery for Effective Cancer Therapy. ACS Nano. 2014; 8: 6922-6933.
46. Sun ZB, Xie HH, Tang SY, et al. Ultrasmall Black Phosphorus Quantum Dots: Synthesis and Use as Photothermal Agents. Angew Chem Int Ed Engl. 2015; 127: 11688-11692.
47. Shubayev VI, Pisanic TR, Jin SH. Magnetic nanoparticles for theragnostics. Adv Drug Deliv Rev. 2009; 61: 467-477.
48. Jung CW, Jacobs P. Physical and chemical properties of superparamagnetic iron oxide MR contrast agents: ferumoxides, ferumoxtran, ferumoxsil. Magn Reson Imaging. 1995; 13: 661-674.